An analytical solution to the dispersion-by-inversion problem in magnetic resonance elastography

Joaquin Mura[1] | **Felix Schrank[2]** 🆔 | **Ingolf Sack[2]** 🆔

[1]Department of Mechanical Engineering, Universidad Técnica Federico Santa María, Santiago, Chile

[2]Department of Radiology, Charité - Universitätsmedizin Berlin, Germany

Correspondence
Ingolf Sack, Department of Radiology,
Charité - Universitätsmedizin Berlin,
Charitéplatz 1, 10117 Berlin, Germany.
Email: ingolf.sack@charite.de

Funding information
Deutsche Forschungsgemeinschaft,
Grant/Award Number: GRK2260, BIOQIC
and SFB1340 Matrix-in-Vision

Purpose: Magnetic resonance elastography (MRE) measures stiffness of soft tissues by analyzing their spatial harmonic response to externally induced shear vibrations. Many MRE methods use inversion-based reconstruction approaches, which invoke first- or second-order derivatives by finite difference operators (first- and second-FDOs) and thus give rise to a biased frequency dispersion of stiffness estimates.

Methods: We here demonstrate analytically, numerically, and experimentally that FDO-based stiffness estimates are affected by (1) noise-related underestimation of values in the range of high spatial wave support, that is, at lower vibration frequencies, and (2) overestimation of values due to wave discretization at low spatial support, that is, at higher vibration frequencies.

Results: Our results further demonstrate that second-FDOs are more susceptible to noise than first-FDOs and that FDO dispersion depends both on signal-to-noise ratio (SNR) and on a lumped parameter *A*, which is defined as wavelength over pixel size and over a number of pixels per stencil of the FDO. Analytical FDO dispersion functions are derived for optimizing *A* parameters at a given SNR. As a simple rule of thumb, we show that FDO artifacts are minimized when *A*/2 is in the range of the square root of 2SNR for the first-FDO or cubic root of 5SNR for the second-FDO.

Conclusions: Taken together, the results of our study provide an analytical solution to a long-standing, well-recognized, yet unsolved problem in MRE postprocessing and might thus contribute to the ongoing quest for minimizing inversion artifacts in MRE.

KEYWORDS
direct inversion, finite difference operators, Helmholtz equation, MRE, multifrequency magnetic resonance elastography, shear wave speed dispersion, wave phase gradient

1 | INTRODUCTION

Magnetic resonance elastography (MRE) measures viscoelastic shear properties of biological soft tissues in vivo using externally induced vibrations at different frequencies to capture the tissue's local harmonic response by motion-sensitive magnetic resonance imaging (MRI). MRE has been proven to be sensitive to many diseases including liver fibrosis,[1] liver tumors,[2-4] renal dysfunction,[5] and neuroinflammation.[6]

MRE generates parameter maps from time-harmonic shear wavefields using inverse problem solutions.[7] Inverse methods in MRE published in the literature differ by their treatment of noise, boundary conditions, and tissue properties including heterogeneity, compressibility, anisotropy, and viscosity.[8-13] Nonetheless, most MRE inversion methods are similar in that they yield parameter maps with a spatial resolution above the diffraction limit, thus providing super-resolution. To achieve this, fine features of the curvature of shear waves are analyzed, often by applying finite-difference operators (FDOs) to the wave images.[14] FDOs can retrieve the spatial gradient of the wave image with pixel-wise resolution.[15]

Inversion techniques that solve the wave equation in MRE (Helmholtz equation) rely on second-order FDOs (second-FDOs), or the Laplacian, whereas other techniques rely on the phase gradient of propagating plane waves and use only first-order FDOs (first-FDOs). First-FDO methods provide wave numbers, which are inversely proportional to shear wave speed c.[16] By contrast, second-FDO inversion (Helmholtz inversion or direct inversion) yields shear modulus, which is related to c^2.[7] Despite their different physical units, shear modulus and shear wave speed are used in the literature as parameters of tissue stiffness at vibration frequency.[17] Henceforth, the term *stiffness* is used when discussing the qualitative changes in c and c^2 that occur with frequency (dispersion).

Tissue-intrinsic dispersion of stiffness is determined by the material's viscoelastic behavior. A purely elastic material has no dispersion, yielding constant stiffness values over frequency. However, it has been recognized that intrinsic dispersion recovered by FDO methods is subject to bias.[18-20] Specifically, we and others have shown that stiffness is likely to be overestimated at low spatial support due to the discretization of shear waves while it is often underestimated at high spatial support due to noise.[18,19] Because spatial support in MRE is the number of pixels per wavelength (wave number times pixel size or wavelength divided by pixel size), multifrequency MRE examinations automatically result in a variation of spatial support due to the occurrence of different wavelengths. Consequently, FDO-based inversion approaches can result in an artificial dispersion of stiffness over frequency, which is superposed to the intrinsic dispersion caused by tissue viscosity.

This well-known *dispersion-by-inversion* problem in MRE has never been analytically solved in a closed form for first- and second-order FDO approaches with consideration of both discretization and noise. Instead, earlier investigators proposed spatial support of 6 to 9 pixels per wavelength to avoid discretization artifacts[18,19] without taking into account SNR, kernel width (or type of the stencil[21]), and order of FDOs. We here provide this information, validate our analytical solution of the *dispersion-by-inversion* problem by numerical simulations as well as phantom data, and derive a simple rule of thumb for minimizing FDO-related dispersion artifacts for future MRE examinations.

2 | THEORY

In this section, we first outline the analytical responses of FDOs to data containing either discretized harmonic waves or pure Gaussian noise. We then continue by combining both signals into master equations of FDO-related dispersion functions for defining the range of unbiased MRE inversions.

2.1 | Discretization

Finite differences can be approximated by Taylor series expansions of $O(h^n)$ with $n > 1$ and $h = N \cdot d$, where d is the pixel size and $N \geq 1$ is the width of the kernel measured in number of pixels (eg, with $N = 1$, derivatives are computed across adjacent pixels without gap). $O(h^2)$-expansions of central first- and second-order derivatives in one-dimensional image space (x) can be represented on the basis of Dirac distributions $\delta(x)$[15]:

$$^1\text{FDO} = \frac{\delta\left(x + \frac{Nd}{2}\right) - \delta\left(x - \frac{Nd}{2}\right)}{Nd} + \frac{(Nd)}{2}\frac{\partial^2}{\partial x^2} \quad (1)$$

$$^2\text{FDO} = \frac{\delta(x + Nd) - 2\delta(x) + \delta(x - Nd)}{(Nd)^2} + (Nd)\frac{\partial^3}{\partial x^3}. \quad (2)$$

^{1}FDO and ^{2}FDO denote central first- and second-order finite difference kernels, respectively, which are typically used in MRE inversion techniques.[13,15] Central difference operators are often applied in MRE because other nonsymmetric stencils neglect information from one direction. Furthermore, $O(h^n)$ operators with $n = 2$ have been proven relatively stable whereas higher order approximations of $n > 2$ result in unwanted oscillations in the presence of noise due to Runge's phenomenon.[22] Henceforth, we restrict our attention to ^{1}FDO and ^{2}FDO approximations given by the first terms on the right hand sides in Equations (1) and (2) (neglecting the remainders). These central difference FDOs are used in many MRE inversion techniques including multifrequency inversions, MDEV (^{2}FDO),[23] and k-MDEV (^{1}FDO).[16]

Given infinite support, Equation (1) or (2) applied to harmonic waves of wavenumber k_0 provide their first or second spatial derivatives and thus result in phase-shifted waves, which are scaled by k_0 or k_0^2, respectively. At finite support, the harmonic responses ($k_{harmonic}$) of ^{1}FDO and ^{2}FDO can be obtained by Fourier transformation of Equations (1) and (2) with respect to x, yielding:

$$ {}^1k_{harmonic} = \frac{1}{Nd\pi} \left| \sin \left(\frac{\pi}{A} \right) \right| \quad \text{(for first-FDO)} \quad (3)$$

$$ {}^2k_{harmonic} = \left(\frac{1}{Nd\pi} \left| \sin \left(\frac{\pi}{A} \right) \right| \right)^2 \quad \text{(for second-FDO)} \quad (4)$$

with

$$ A = \frac{1}{Ndk_0} = \frac{wavelength}{pixel\ size \cdot kernel\ width}. \quad (5)$$

A is the key parameter of the resolution of wave images in MRE. Similar to the Nyquist limit, it determines when aliasing of wave numbers occurs due to low spatial support and

FDO kernel sizes. As seen in Figure 1, $A < 2$ (ie, $dk_0N > 0.5$), this is the spatial support below 2 pixels per wavelength signifies the limit of ambiguous derivatives because Equations (3) and (4) are symmetric around $A = 2$.

As such, A determines the artifacts caused by discretization in FDO-based MRE inversion. The second important variable is SNR. Larger pixels and wider derivative kernels minimize the noise susceptibility of the apparent wave number k obtained by FDO. Henceforth, we account for the expectation values of FDO when applied to noise in order to find the optimal A.

2.2 | Noise

As further detailed in the Appendix, a complex-valued variable $Z = X + iY$ with X and Y being randomly scattered with Gaussian distribution of variance σ^2 and zero mean has the following expectation values:

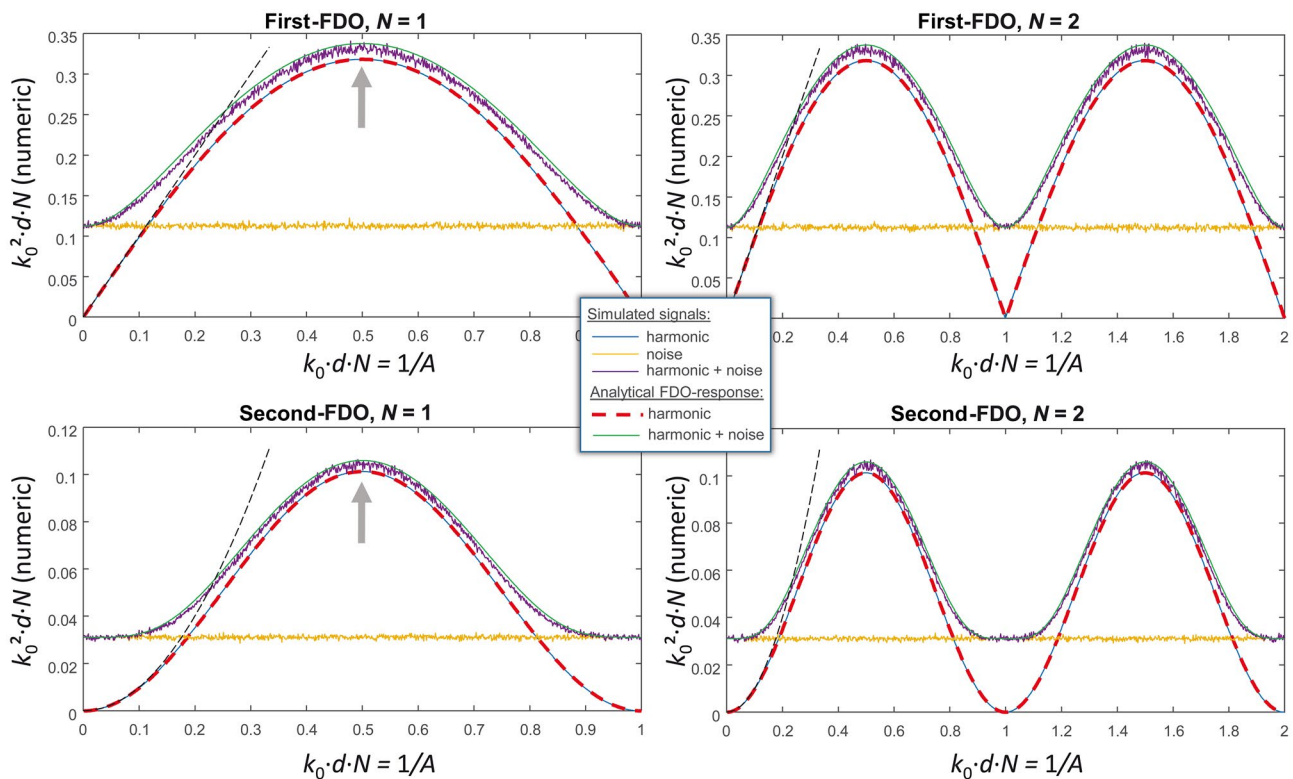$$ E(|X|) = E(|Y|) = \sigma \sqrt{\frac{2}{\pi}} \quad (6)$$

FIGURE 1 Amplitude (wavenumber) responses of finite difference operators of first (first-FDO) and second order (second-FDO). Shown are numerical FDO responses to the following simulated signals: (A) harmonic $u^* = \exp(ik_0r)$ (blue), (B) pure complex Gaussian noise based on Matlab's *randn* function (u^*_{noise}, yellow), and (C) superposed signals of (A) and (B) ($u^* + u^*_{noise}$, dark purple, signal-to-noise ratio [SNR] = 2). Additionally, analytical signals are plotted, (D) for ${}^1k_{harmonic}$ (first-FDO) and ${}^2k_{harmonic}$ (second-FDO) of Equations (3) and (4) (dashed, red) as well as (E) for ${}^nk = \sqrt{({}^nk_{harmonic})^2 + ({}^nk_{noise})^2}$ of Equation (13) (green). Black dashed lines indicate ideal FDO properties of infinitely narrow kernels, that is, linear for first derivatives and quadratic for second derivatives. Note that (A) and (D) are visually identical. Arrows indicate the limits of $A < 2$ or $dk_0N > 0.5$ (corresponding to spatial supports of less than two pixels per wavelength) when aliased FDO derivatives are obtained (Nyquist limit of FDOs)

$$E(|Z|) = \sigma \sqrt{\frac{\pi}{2}} \tag{7}$$

$$E\left(\left|{}^1FDO(Z)\right|\right) = \frac{\sigma}{Nd}\sqrt{\pi} \tag{8}$$

$$E\left(\left|{}^2FDO(Z)\right|\right) = \frac{\sigma}{(Nd)^2}\sqrt{3\pi} \tag{9}$$

We assume that Z is the noisy part of a complex harmonic function (signal) with normalized amplitude leading to an SNR of $1/E(|Z|)$.[24] Thus, according to Equation (7), SNR reads

$$SNR = \frac{1}{\sigma}\sqrt{\frac{2}{\pi}}. \tag{10}$$

The corresponding wavenumbers obtained by FDO that were applied to pure noise Z are given as

$${}^1k_{noise} = \sigma\sqrt{\pi}\frac{1}{2\pi Nd} = \frac{\sqrt{2}}{SNR}\frac{1}{2\pi Nd} \quad \text{(for first-FDO)} \tag{11}$$

$$SNR = \sqrt{\frac{3}{8}} \frac{A_0^2}{\sqrt{A_0^4\left(-\sin^2\frac{\pi}{A_0} + \cos^2\frac{\pi}{A_0} - \cos^4\frac{\pi}{A_0}\right) + \pi^4}} \quad \text{(for second-FDO)} \tag{17}$$

$${}^2k_{noise} = \sigma\sqrt{3\pi}\left(\frac{1}{2\pi Nd}\right)^2 = \frac{\sqrt{5}}{SNR}\left(\frac{1}{2\pi Nd}\right)^2 \quad \text{(for second-FDO)} \tag{12}$$

2.3 | Discretization and noise

Apparent wave numbers ${}^nk$ with $n = 1,2$ for first- and second-order FDOs, respectively, are the Euclidian norm of harmonic signal and noise:

$${}^nk = \sqrt{\left({}^nk_{harmonic}\right)^2 + \left({}^nk_{noise}\right)^2}. \tag{13}$$

Figure 1 illustrates the effect of overestimation of ${}^nk$ in noisy signals, which in turn leads to the underestimation of stiffness (c) at high support (high A). In Figure 2, the dispersion functions of normalized stiffness (c normalized by true c_0) are given by $\frac{c}{c_0} = \frac{k_0}{{}^1k}$ and $\left(\frac{c}{c_0}\right)^2 = \frac{k_0^2}{{}^2k}$ for first- and second-FDOs, respectively, and plotted versus $d \cdot k_0$ (the ratio of wavelength over pixel size) in Figure 2A,B for $N = 1, 2, …, 5$. Stiffness values are correctly estimated when the curves cross $c/c_0 = 1$. The position of these intercepts on the $d \cdot k_0$-axis depends on N such that higher spatial support is required for larger FDO kernel sizes. Figure 2C shows master curves of normalized shear wave speed for first- and second-FDOs versus A, into which all curves from Figure 2A,B collapse. Inflection points where both master curves equal 1, ie, ${}^1A_0 = \frac{1}{Ndk_0}$ with $k_0 = {}^1k$ and ${}^2A_0 = \frac{1}{Ndk_0}$ with $k_0 = \sqrt{{}^2k}$, can be derived analytically. Therefore, we insert the harmonic signals of Equations (3) or (4) and noise given by Equations (11) or (12) into Equation (13) that is then solved for the inflection point A_0 as follows:

$$A_0^2 = \frac{\pi^2}{\sin^2\frac{\pi}{A_0} + \frac{1}{2}\frac{1}{SNR}} \quad \text{(for first-FDOs)} \tag{14}$$

$$A_0^4 = \frac{\pi^4}{\sin^2\frac{\pi}{A_0} - \cos^2\frac{\pi}{A_0} + \cos^4\frac{\pi}{A_0} + \frac{3}{8}\frac{1}{SNR^2}}. \quad \text{(for second-FDOs)} \tag{15}$$

These equations cannot be solved directly for A_0 but are solved for SNR instead:

$$SNR = \frac{A_0}{\sqrt{2\pi^2 - 2A_0^2\sin^2\frac{\pi}{A_0}}} \quad \text{(for first-FDO)} \tag{16}$$

Both functions, plotted in Figure 3 in the range of $A_0 = 1, 2, …, 100$, represent rather simple powerlaws in that range of A-values. Consequently, good approximations can be obtained by series expansion. Series expansion up to second and third orders lead to numerical approximations of $SNR \approx \frac{A_0^2}{8}$ and $SNR \approx \frac{A_0^3}{40}$ for Equations (16) and (17), respectively, as shown in Figure 3. The corresponding functions $A_0(SNR)$ are readily obtained by

$$A_0 \approx 2\sqrt{2SNR} \quad \text{(for first-FDOs)} \tag{18}$$

$$A_0 \approx 2\sqrt[3]{5SNR} \quad \text{(for second-FDOs)} \tag{19}$$

At a given SNR, these A-values indicate kernel sizes and pixel widths and provide values near ground truth in FDO-based MRE inversion.

3 | METHODS

3.1 | Experimental setup

Multifrequency MRE was investigated using an elastic, homogenous phantom made available to the MRE study group
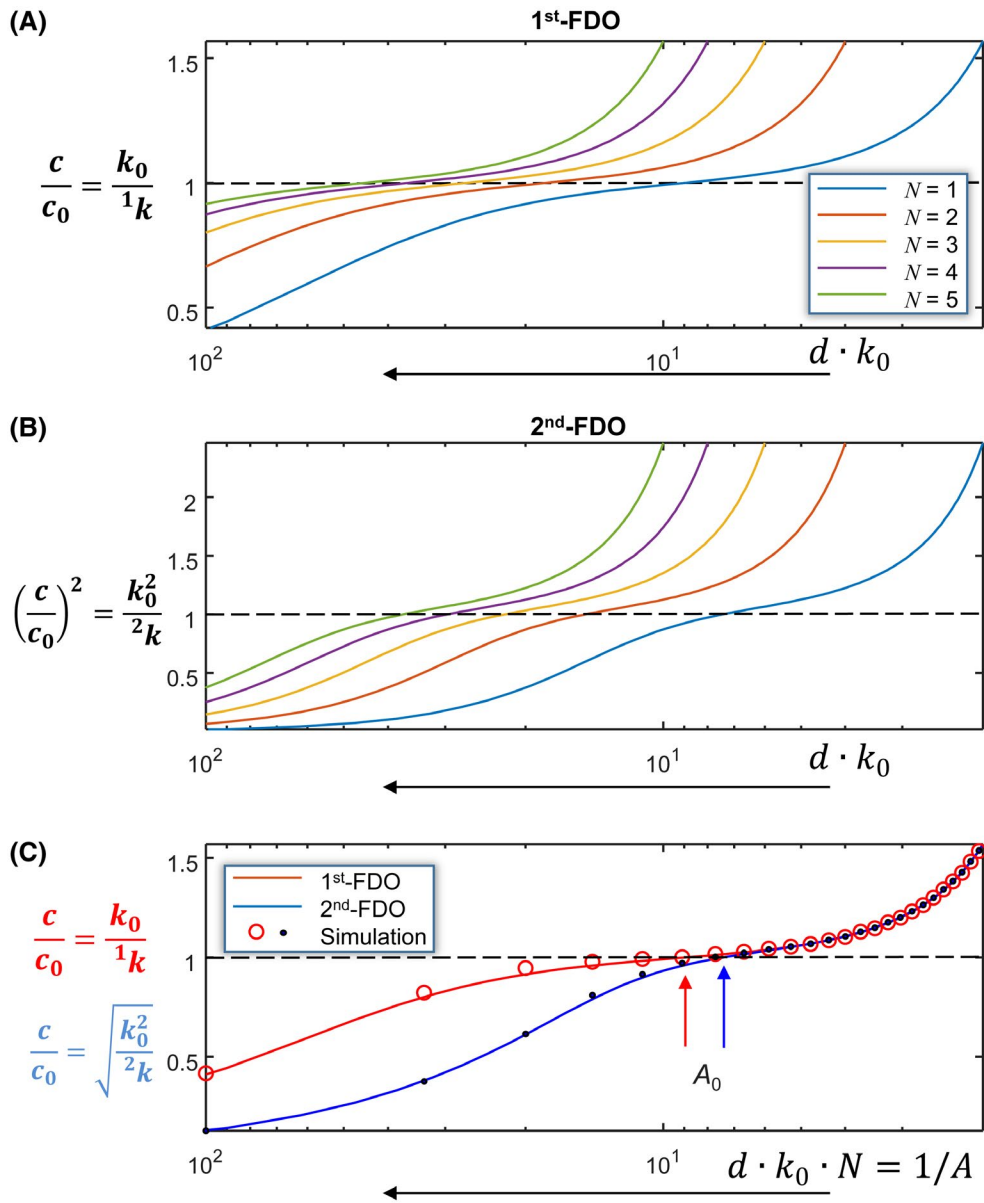
FIGURE 2 Analytical *dispersion-by-inversion* by first- (A) and second- (B) order finite difference operators (FDOs) of different stencil sizes $N = 1$ to 5 and signal-to-noise ratio (SNR) = 10 according to Equation (13). Note that the x-axes in (A) and (B) (pixels per wavelength or $d \cdot k_0$) are reversed in order to indicate the increase in values with increasing vibration frequency (frequency dispersion). The master curves of normalized shear wave speed for first-FDO (red) and second-order FDOs (blue) versus A are shown in (C) along with numerical simulations of noisy, harmonic signals and numerical FDOs of $N = 1$ to 5 (red, open circles for first-FDOs, blue dots for second-FDOs). Inflection points where $A = A_0$ are indicated by red and blue vertical arrows for first- and second-FDOs according to Equations (18) and (19), respectively. These points correspond to the analytical solutions shown in Figure 3

of the ISMRM by Resoundant Inc. (Rochester, Minnesota, USA) in 2016. The phantom is made from a homogeneous elastic material permanently sealed in a high impact container. The stiffness value for this phantom provided by the manufacturer are between 2.0 kPa and 4.0 kPa and are expected to increase slightly (5%-10%) per year. Data were acquired in a 1.5 Tesla MRI scanner (Siemens, Magnetom Sonata) using the standard head coil and a single-shot spin-echo echo-planar imaging sequence with a bipolar motion-encoding gradient of 20 mT/m amplitude.[25] Vibrations from

50 to 150 Hz frequency were induced by an external piezoe-lectric driver mounted to a rigid rod for wave transmission,[23] resulting in concentrically emanating waves for the wave component, which was polarized through the plane. Five slices were acquired in an axial view through the center part of the cylindrical phantom vessel. Further imaging parameters were repetition time (TR) = 2000 ms, time to echo (TE) = 69 ms, flip angle = 90°, field of view = 288 × 240 mm², matrix size = 96 × 80 (pixel size d = 1.9 × 1.9 mm²), and slice thickness = 1.9 mm.
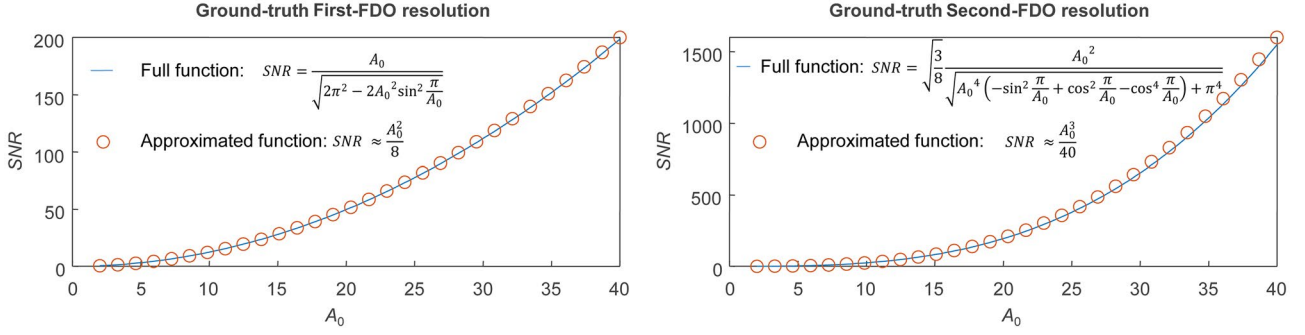
Ground-truth First-FDO resolution

Full function: $SNR = \dfrac{A_0}{\sqrt{2\pi^2 - 2A_0^2 \sin^2 \frac{\pi}{A_0}}}$

Approximated function: $SNR \approx \dfrac{A_0^2}{8}$

Ground-truth Second-FDO resolution

Full function: $SNR = \sqrt{\dfrac{3}{8}} \dfrac{A_0^2}{\sqrt{A_0^4 \left(-\sin^2 \frac{\pi}{A_0} + \cos^2 \frac{\pi}{A_0} - \cos^4 \frac{\pi}{A_0}\right) + \pi^4}}$

Approximated function: $SNR \approx \dfrac{A_0^3}{40}$

FIGURE 3 Approximated and full functions of signal-to-noise ratio (*SNR*) versus A_0 according to Equations (18) and (19)
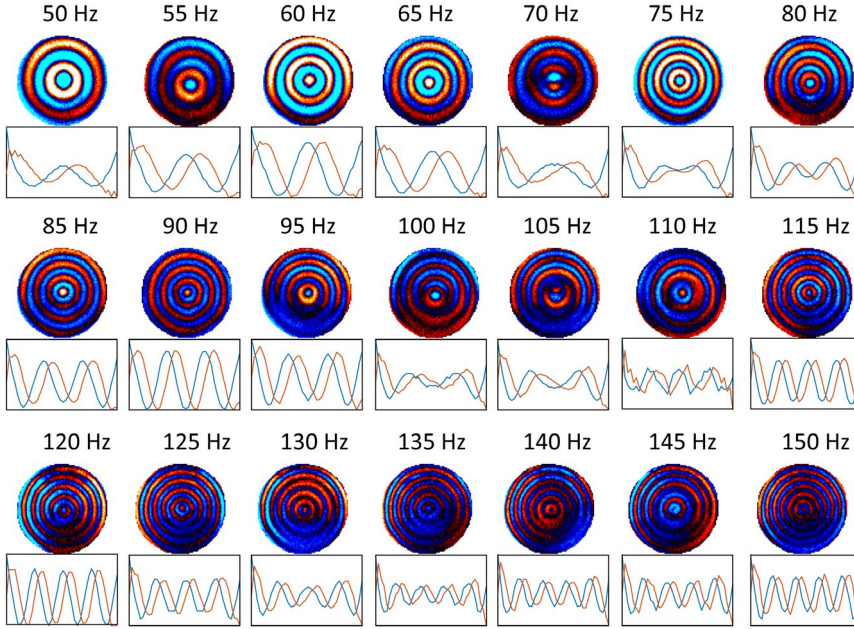

FIGURE 4 Experimental wave images and wave profiles at 21 driving frequencies. Wave images show through-plane wave components (real part of temporally Fourier-transformed waves at vibration frequency). Graphs below the wave images depict profiles along the radius of the cylindrical waves, averaged over the azimuthal angle and filtered as described in the Methods section. Real- and imaginary parts of the complex-valued wave profiles are plotted in blue and red, respectively

3.2 | Experimental data evaluation

The experimentally acquired concentric wave patterns were unwrapped and Fourier-transformed in time to extract complex-valued wave images at driving frequency f as shown in Figure 4. These wave images were mapped onto cylindrical coordinates and averaged over the azimuthal angle, resulting in a single wave profile $u^*(r,f)$ along the radial coordinate r (see Figure 4). The obtained one-dimensional profiles were used to demonstrate FDO inversion in experimental data. As in numerical simulations, FDO stencils were generated in Matlab by [−1, 1], [1, −2, 1] for first- and second-FDOs of $N = 1$, and [−1, 0, 1], [1, 0, −2, 0, 1] for $N = 2$, [−1, 0, 0, 1], [1, 0, 0, −2, 0, 0, 1] for $N = 3$ etc. These kernels were applied to $u^*(r,f)$ using Matlab's conv function. SNR was determined by taking the amplitude of the fundamental spatial frequency over the averaged amplitudes of all higher harmonic frequencies, which we treated as noise.

Ground truth shear wave speed c_0 was reconstructed without differential operators in order to avoid stiffness biases due to discretization and noise artifacts as theoretically analyzed in the previous section. Therefore, c_0 values were determined by fitting Bessel functions to $u^*(r,f)$ assuming that the shear waves are polarized along the infinitely large cylinder axis[26-28]:

$$u^* = u_0 \frac{J_0\left(k_0^* r\right)}{J_0\left(k_0^* R\right)} e^{i\psi} + O^*. \tag{20}$$

J_0 denotes the Bessel function of first kind, u_0 is the wave amplitude, ψ is the phase of the shear wave at sample radius $r = R$, and O^* is a complex-valued offset term that accounts for compression waves. k_0^*, the ground truth complex-valued wave number, was the desired result of the fit and was converted to shear wave speed by $c_0 = f / Re\left(k_0^*\right)$.

4 | RESULTS

Numerical results of FDOs applied to simulations of complex oscillations $u^* = \exp\left(ik_0 r\right)$ with added complex noise,

which was generated using Matlab's *randn* function, are shown in Figure 2C. The analytical solutions given in Equation (13) agree with numerical simulations. For this
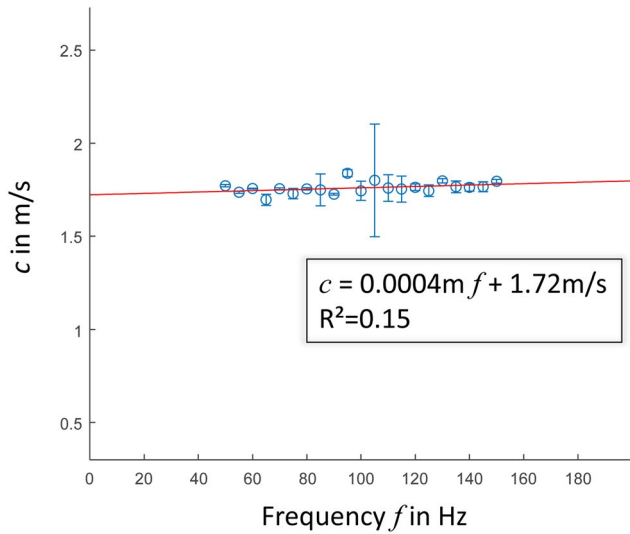

FIGURE 5 Experimental shear wave speeds over frequency derived from Bessel fits with linear regression

master curve, second-FDO results are given as wave speed c/c_0 instead of $(c/c_0)^2$ in order to demonstrate the alignment of first- and second-FDO results at low support, that is, in the range of discretization bias ($c/c_0 > 1$). Figure 2C also demonstrates the excellent prediction of inflection point A_0 by Equations (18) and (19), allowing the further use of these approximates for minimization of inversion biases in FDO-based MRE reconstruction.

Figure 5 shows ground truth shear wave speed values of the phantom over frequencies. The values obtained by analytical fits display no significant dispersion over frequency, as illustrated by the linear regression function of 0.0004 m/s/Hz slope and $c_0 = 1.72$ m/s ($R^2 = 0.15$, P value = .08).

Figure 6 demonstrates the relative overestimation as well as undershot of c/c_0 (first-FDO) and $(c/c_0)^2$ (second-FDO) due to discretization and noise in experimental data. Colors encode different stencil widths from $N = 1$ to 5. Analytical curves were calculated by Equation (13) based on Equations (3) and (4) for $k_{harmonic}$ and Equations (11) and (12) for k_{noise} using the experimental pixel size $d = 1$ mm and *SNR* values given in Table 1. Fluctuations in analytical signals visible at higher *A*-values (kernel size $N = 1$) resulted from SNR
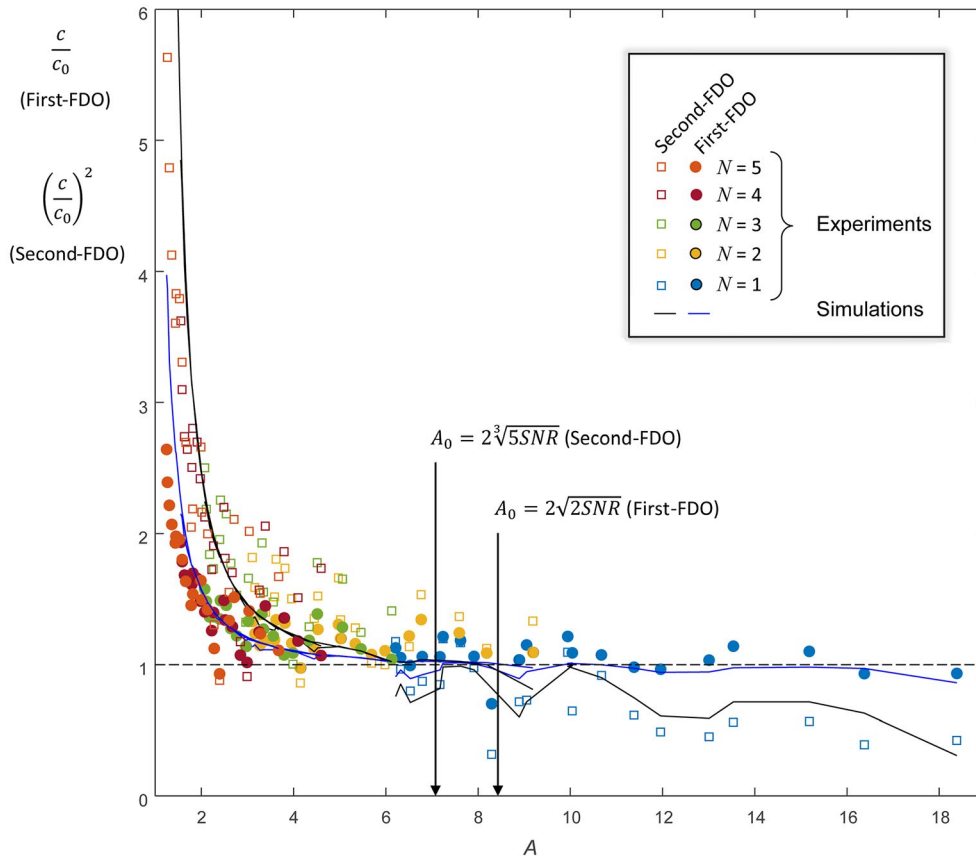

FIGURE 6 Experimental shear wave speed recovered by first-finite difference operators (FDOs) (c, closed circles) and second-FDOs (c^2, open squares) of $N = 1$ (blue), 2 (yellow), 3 (green), 4 (orange), and 5 (dark red) and normalized with c_0 from Figure 5 and Table 1 versus A. Analytical curves (black for second-FDOs, blue for first-FDOs) were calculated based on c_0 and signal-to-noise ratio (*SNR*), both given in Table 1. Variations in analytical curves are mainly due to variations in *SNR* over frequency. Vertical arrows indicate the solutions of A_0 according to Equations (18) and (19) taking the mean *SNR* of all frequencies from Table 1

#	Frequency in Hz	c in m/s	c (SD) in m/s	Wavelength/pixel size	SNR
1	50	1.77	0.01	18.4	6.9
2	55	1.74	0.01	16.4	13.7
3	60	1.76	0.00	15.2	14.8
4	65	1.70	0.03	13.5	11.7
5	70	1.76	0.00	13.0	7.8
6	75	1.73	0.03	12.0	6.9
7	80	1.75	0.01	11.4	9.0
8	85	1.75	0.09	10.7	13.5
9	90	1.72	0.00	9.9	20.6
10	95	1.84	0.02	10.0	23.2
11	100	1.74	0.05	9.1	5.1
12	105	1.80	0.30	8.9	3.7
13	110	1.76	0.07	8.3	5.7
14	115	1.75	0.07	7.9	9.3
15	120	1.76	0.02	7.6	10.3
16	125	1.74	0.03	7.2	8.5
17	130	1.80	0.01	7.2	4.2
18	135	1.77	0.03	6.8	3.1
19	140	1.76	0.02	6.5	2.6
20	145	1.77	0.03	6.3	3.5
21	150	1.79	0.01	6.2	2.6

Abbreviation: SNR, signal-to-noise ratio.

variations in wave profiles $u^*(r,f)$ between different vibration frequencies f. SNR values ranged from 2.6 at 150 Hz to 23.2 at 95 Hz with a mean of 8.9 ± 5.7. Experimental results are summarized in Table 1.

5 | DISCUSSION

This study adds to the ongoing quest for quantitative and reproducible MRE biomarkers that are consistent with ground truth values.[17] Ground truth in MRE is normally provided by shear oscillatory rheometry, which, however, has well-known limitations regarding its sensitivity to surface texture, plate pressure, and sample geometry. Moreover, MRE biomarkers involve inverse problem solutions, which are often ill posed due to noise and unknown boundary conditions, making MRE susceptible to inversion bias.[15] Many inversion methods in MRE methods use FDOs and are known to be biased by discretization and noise.[29] Nevertheless, FDOs are frequently used in MRE due to their simple implementation, computational power, and their robustness against local stiffness changes (heterogeneity) and variation in tissue geometry and morphology. As a result, competing over- and underestimates of FDO signals occur at the same time, giving rise to an inflection point (A_0) at which the stiffness dispersion curve coincides with ground truth values. This synchrony of over- and undershooting effects is the reason why second-FDOs, which are highly sensitive to noise, require smaller A_0 values than first-FDOs. However, considering SNR to be typically in the range of 1 to 100, the relative difference in A_0 between first- and second-FDOs is relatively small (eg, $A_0 = 9.2$ versus 12.4 for $SNR = 10$ and $N = 1$). In practice, approximated values of A_0 rather than precise values should be taken into account. For instance, when A_0 is more than an integer factor larger than recommended values, N should be increased in order to decrease the noise sensitivity of the FDO used.

It should be noted that many MRE inversion methods treat noise using k-space filters or wavelets prior to FDOs of constant kernel widths[7,14] or apply Savitsky-Golay filters in order to combine second derivatives with denoising by polynomial regression.[7] Effectively, these strategies can provide the same smoothing as an adaptation of N but naturally vary in technical details and are thus difficult to analyze with an explicit estimation of the error as we do here. Therefore, we focused, in theory, on unsmoothed raw wave data $u^*(r,f)$ assuming white Gaussian noise and analyzed the effect of noise suppression by FDO kernel size. Clearly, noise, as defined as unwanted signal in MRE,[15] can have different sources including compression waves[30] or slice jittering[31] making noise anisotropic and non-Gaussian.

Furthermore, SNR given by σ in this study is normally addressed by other methods such as octahedral shear strain,[24] shear strain invariant noise,[32] or wavelet-based methods,[29] all of which provide values different from those obtained by Equation (10). Our method of normalizing the fundamental vibration signal with higher harmonic noise agrees remarkably well with Gaussian SNR and, thus, also with the predicted dispersion functions. However, it should be mentioned that this strategy is only feasible in homogenous materials of single spatial frequency while limited in vivo. Our phantom data are not meant to reproduce in vivo soft tissue properties but to present ground truth wave speed c_0 values without frequency dependence. A drawback of the absence of viscosity is that undamped waves resulted in multidirectional k-vectors, which we treated by directional filtering as proposed in,[33] although classical Helmholtz inversion (second-order FDO inversion) does not require such directional filtering. Finally, our study was restricted to one-dimensional analysis. Again, the aim of this study was to develop the basic layout of an inversion-by-dispersion analysis in a mathematically consistent manner. Higher-dimensional FDO methods can be used to efficiently suppress noise[34] or to address stiffness heterogeneities by employing finite volumes.[35]

In summary, we have introduced an analytical approach to the well-known dispersion-by-inversion bias in MRE. Using closed-form solutions, numerical simulations, and phantom experiments, we demonstrate that FDO-based stiffness estimates can be affected by simultaneous under- and overestimation of values due to the presence of noise and wave signal discretization, respectively. Our results further show that second-order FDOs are more sensitive to noise and are more markedly biased by discretization than first-order FDOs. A lumped parameter A was introduced, which defines spatial support of the shear waves including stencil width of FDOs. Analytical FDO dispersion functions were analytically derived, and simple rules of thumb are provided, which might help to minimize FDO-related inversion artifacts in future examinations. This study adds to research on inversion artifacts in MRE and may contribute to more reliable viscoelasticity reconstruction in future multifrequency MRE examinations.

ACKNOWLEDGMENTS

ORCID
Felix Schrank https://orcid.org/0000-0001-6535-8597
Ingolf Sack https://orcid.org/0000-0003-2460-1444

REFERENCES

1. Venkatesh SK, Yin M, Ehman RL. Magnetic resonance elastography of liver: Technique, analysis, and clinical applications. *J Magn Reson Imaging*. 2013;37:544–555.
2. Venkatesh SK, Yin M, Glockner JF, et al. MR elastography of liver tumors: Preliminary results. *AJR Am J Roentgenol*. 2008;190:1534–1540.
3. Garteiser P, Doblas S, Daire JL, et al. MR elastography of liver tumours: Value of viscoelastic properties for tumour characterisation. *Eur Radiol*. 2012;22:2169–2177.
4. Shahryari M, Tzschatzsch H, Guo J, et al. Tomoelastography distinguishes noninvasively between Benign and Malignant liver lesions. *Cancer Res*. 2019;79:5704–5710.
5. Marticorena Garcia SR, Grossmann M, Bruns A, et al. Tomoelastography paired with T2* magnetic resonance imaging detects lupus nephritis with normal renal function. *Invest Radiol*. 2019;54:89–97.
6. Wuerfel J, Paul F, Beierbach B, et al. MR-elastography reveals degradation of tissue integrity in multiple sclerosis. *NeuroImage*. 2010;49:2520–2525.
7. Manduca A, Oliphant TE, Dresner MA, et al. Magnetic resonance elastography: Non-invasive mapping of tissue elasticity. *Med Image Anal*. 2001;5:237–254.
8. Romano AJ, Shirron JJ, Bucaro JA. On the noninvasive determination of material parameters from a knowledge of elastic displacements theory and numerical simulation. *IEEE Trans Ultrason Ferroelectr Freq Control*. 1998;45:751–759.
9. Kolipaka A, McGee KP, Manduca A, et al. Magnetic resonance elastography: Inversions in bounded media. *Magn Reson Med*. 2009;62:1533–1542.
10. Doyley MM. Model-based elastography: A survey of approaches to the inverse elasticity problem. *Phys Med Biol*. 2012;57:R35–73.
11. Honarvar M, Sahebjavaher RS, Rohling R, Salcudean SE. A comparison of finite element-based inversion algorithms, local frequency estimation, and direct inversion approach used in MRE. *IEEE Trans Med Imaging*. 2017;36:1686–1698.
12. Solamen LM, McGarry MD, Tan L, Weaver JB, Paulsen KD. Phantom evaluations of nonlinear inversion MR elastography. *Phys Med Biol*. 2018;63:145021.
13. Fovargue D, Nordsletten D, Sinkus R. Stiffness reconstruction methods for MR elastography. *NMR Biomed*. 2018;31:e3935.
14. Barnhill E, Hollis L, Sack I, et al. Nonlinear multiscale regularisation in MR elastography: Towards fine feature mapping. *Med Image Anal*. 2017;35:133–145.
15. Hirsch S, Braun J, Sack I. *Magnetic Resonance Elastography: Physical Background And. Medical Applications*. Weinheim: Wiley-VCH; 2017.
16. Tzschatzsch H, Guo J, Dittmann F, et al. Tomoelastography by multifrequency wave number recovery from time-harmonic propagating shear waves. *Med Image Anal*. 2016;30:1–10.
17. Manduca A. MR elastography: Standardizing terminology and setting guidelines. In Proceedings of the 1st International MRE Workshop, Berlin, Germany, 2017:12.
18. Papazoglou S, Hamhaber U, Braun J, Sack I. Algebraic Helmholtz inversion in planar magnetic resonance elastography. *Phys Med Biol*. 2008;53:3147–3158.
19. Arunachalam SP, Rossman PJ, Arani A, et al. Quantitative 3D magnetic resonance elastography: Comparison with dynamic mechanical analysis. *Magn Reson Med*. 2016;77:1184–1192.

20. Yue JL, Tardieu M, Julea F, et al. Acquisition and reconstruction conditions in silico for accurate and precise magnetic resonance elastography. *Phys Med Biol*. 2017;62:8655–8670.

21. Langtangen HP, Linge S. *Finite Difference Computing with PDEs: A Modern Software Approach (Texts in Computational Science and Engineering (16))*. Springer Open; 2017.

22. Trefethen LN. *Approximation Theory and Approximation Practice*. Philadelphia: Society for Industrial and Applied Mathematics; 2012.

23. Hirsch S, Guo J, Reiter R, et al. MR elastography of the liver and the spleen using a piezoelectric driver, single-shot wave-field acquisition, and multifrequency dual parameter reconstruction. *Magn Reson Med*. 2014;71:267–277.

24. McGarry MDJ, Van Houten EEW, Perrinez PR, Pattison AJ, Weaver JB, Paulsen KD. An octahedral shear strain-based measure of SNR for 3D MR elastography. *Phys Med Biol*. 2011;56:N153–N164.

25. Dittmann F, Hirsch S, Tzschatzsch H, Guo J, Braun J, Sack I. In vivo wideband multifrequency MR elastography of the human brain and liver. *Magn Reson Med*. 2016;76:1116–1126.

26. Braun J, Tzschatzsch H, Korting C, et al. A compact 0.5 T MR elastography device and its application for studying viscoelasticity changes in biological tissues during progressive formalin fixation. *Magn Reson Med*. 2018;79:470–478.

27. Yasar TK, Royston TJ, Magin RL. Wideband MR elastography for viscoelasticity model identification. *Magn Reson Med*. 2013;70:479–489.

28. Okamoto RJ, Clayton EH, Bayly PV. Viscoelastic properties of soft gels: Comparison of magnetic resonance elastography and dynamic shear testing in the shear wave regime. *Phys Med Biol*. 2011;56:6379–6400.

29. Bertalan G, Guo J, Tzschatzsch H, et al. Fast tomoelastography of the mouse brain by multifrequency single-shot MR elastography. *Magn Reson Med*. 2019;81:2676–2687.

30. Lin K, McLaughlin J. An error estimate on the direct inversion model in shear stiffness imaging. *Inverse Prob*. 2009;25:075003.

31. Barnhill E, Nikolova M, Ariyurek C, Dittmann F, Braun J, Sack I. Fast robust dejitter and interslice discontinuity removal in MRI Phase acquisitions: Application to magnetic resonance elastography. *IEEE Trans Med Imaging*. 2019;38:1578–1587.

32. Sahebjavaher RS, Nir G, Honarvar M, et al. MR elastography of prostate cancer: Quantitative comparison with histopathology and repeatability of methods. *NMR Biomed*. 2015;28:124–139.

33. Manduca A, Lake DS, Kruse SA, Ehman RL. Spatio-temporal directional filtering for improved inversion of MR elastography images. *Med Image Anal*. 2003;7:465–473.

34. Anderssen RS, Hegland M. For numerical differentiation, dimensionality can be a blessing!. *Math Comput*. 1999;68:1121–1141.

35. Davies PJ, Barnhill E, Sack I. The MRE inverse problem for the elastic shear modulus. *SIAM Journal on Applied Mathematics*. 2019;79:1367–1388.

APPENDIX

We here briefly derive the expected mean magnitude values of pure Gaussian noise in a complex-valued signal subjected to finite difference operators (FDOs), which yield the first and second derivatives. If a random variable X is normally distributed with mean μ and variance σ^2, usually represented by $X \sim \mathcal{N}\left(\mu, \sigma^2\right)$, its probability density function (pdf) is given by

$$p_X(x) = \frac{1}{\sqrt{2\pi\sigma^2}} e^{-(x-\mu)^2/(2\sigma^2)}, \quad -\infty < x < \infty \quad \text{(A1)}$$

The expectation for the absolute value of the a normally distributed random variable is

$$E(|X|) = \frac{1}{\sqrt{2\pi\sigma^2}} \int_{-\infty}^{\infty} |x| \, p_X(x) \, dx = \frac{1}{\sqrt{2\pi\sigma^2}} \int_{-\infty}^{\infty} |x| \, e^{-(x-\mu)^2/(2\sigma^2)} dx$$
$$= \frac{1}{\sqrt{2\pi\sigma^2}} \left(I_1 + I_2 \right)$$

$$\text{(A2)}$$

where

$$I_1(\mu, \sigma) = \int_{-\infty}^{0} (-x) \, e^{-(x-\mu)^2/(2\sigma^2)} dx \quad \text{(A3)}$$

and

$$I_2(\mu, \sigma) = \int_{0}^{\infty} x e^{-(x-\mu)^2/(2\sigma^2)} dx \quad \text{(A4)}$$

The change of variable $x \mapsto -x$ shows that $I_1(\mu, \sigma) = I_2(-\mu, \sigma)$. For I_2 we have with

$$I_2 = \int_{0}^{\infty} x e^{-(x-\mu)^2/(2\sigma^2)} dx = 2\sigma^2 \int_{0}^{\infty} \frac{x + \mu - \mu}{\sigma\sqrt{2}} e^{-\left(\frac{x-\mu}{\sigma\sqrt{2}}\right)^2} dx$$
$$= 2\sigma^2 \left[\frac{1}{2} \int_{\mu^2/(2\sigma^2)}^{\infty} e^{-s^2} d\left(s^2\right) + \frac{\mu}{\sigma\sqrt{2}} \int_{-\mu^2/(2\sigma^2)}^{\infty} e^{-s^2} ds \right] \quad \text{(A5)}$$
$$= 2\sigma^2 \left[\frac{1}{2} e^{-\mu^2/(2\sigma^2)} + \frac{\mu}{\sigma\sqrt{2}} erfc\left(-\frac{\mu}{\sigma\sqrt{2}}\right) \right]$$

$$erfc(x) = \frac{2}{\sqrt{\pi}} \int_{x}^{\infty} e^{-s^2} ds \quad \text{(A6)}$$

Therefore, in the particular case of $\mu = 0$, we have $I_1 = I_2 = \sigma^2$ and

$$E(|X|) = \sigma\sqrt{\frac{2}{\pi}}. \quad \text{(A7)}$$

A complex random variable is defined by $Z = X + iY$, where $i = \sqrt{-1}$, and X and Y are real-valued random variables. The distribution of a complex random variable is identified with the joint distribution of X and Y. If both X and Y are uncorrelated random variables normally distributed with zero mean and σ^2 variance, the pdf for Z yields

$$
\begin{aligned}
p_Z(z) &= \frac{1}{2\pi\sigma^2} \exp\left(-\frac{1}{2\sigma^2}\left[x^2 + y^2\right]\right) \\
&= \frac{1}{2\pi\sigma^2} \exp\left(-\frac{r^2}{2\sigma^2}\right)
\end{aligned} \tag{A8}
$$

when the polar form of Z is applied, that is, $z = re^{i\theta}$. To calculate the expected value of the magnitude of a complex variable, it is convenient to keep using polar coordinates, because $|z| = r$ on the complex plane. This implies that

$$
E(|Z|) = \frac{1}{2\pi\sigma^2} \int_0^{2\pi} \int_0^{\infty} re^{-r^2/(2\sigma^2)} r\,dr\,d\theta \tag{A9}
$$

Assuming that the change of variable $u = r^2/(2\sigma^2)$ leads to

$$
E(|Z|) = \sigma\sqrt{2} \int_0^{\infty} \sqrt{u}\,e^{-u}\,du = \sigma\sqrt{2}\,\Gamma\left(\frac{3}{2}\right) = \sigma\sqrt{2}\,\frac{\sqrt{\pi}}{2} \tag{A10}
$$

where $\Gamma(x)$ represents the Gamma function evaluated in x. Therefore

$$
E(|Z|) = \sigma\sqrt{\frac{\pi}{2}} \tag{A11}
$$

In particular, if $Z = \sum_{i=1}^{n} a_i Z_i$, then

$$
E\left(\left|\sum_{i=1}^{n} a_i Z_i\right|\right) = \sigma_{\sum_{i=1}^{n} a_i Z_i} \sqrt{\frac{\pi}{2}} \tag{A12}
$$

and applying the following property for variance

$$
\sigma_{\sum_{i=1}^{n} a_i Z_i}^2 = Var\left[\sum_{i=1}^{n} a_i Z_i\right] = \sum_{i=1}^{n} a_i^2 Var\left[Z_i\right] = \sum_{i=1}^{n} a_i^2 \sigma^2 \tag{A13}
$$

implies that

$$
E\left(\left|\sum_{i=1}^{n} a_i Z_i\right|\right) = \sigma\sqrt{\sum_{i=1}^{n} a_i^2} \sqrt{\frac{\pi}{2}} \tag{A14}
$$

which is valid for $Z_1, Z_2, \ldots, Z_n$, which represent pairwise independent random variables with $Z_i \sim \mathcal{N}\left(0, \sigma^2\right)$. Recalling the definition given in Equation (1)

$$
{}^1\text{FDO}(Z) = \frac{1}{Nd}\left(Z_1 - Z_2\right) \tag{A15}
$$

where $Z_1 = X_1 + iY_1$ and $Z_2 = X_2 + iY_2$ are independent and identically distributed (i.i.d.) random variables with zero mean and variance σ^2, which represent two different positions in the imaging plane. Using Equation (A14) we obtain

$$
E\left(\left|{}^1\text{FDO}(Z)\right|\right) = \frac{\sigma}{Nd}\sqrt{2}\sqrt{\frac{\pi}{2}} = \frac{\sigma}{Nd}\sqrt{\pi}. \tag{A16}
$$

Correspondingly, second-order FDOs defined in (2) can be represented as

$$
{}^2\text{FDO}(Z) = \frac{1}{N^2 d^2}\left(Z_1 - 2Z_2 + Z_3\right). \tag{A17}
$$

Again, $Z_j = X_j + iY_j$ is i.i.d for $j = 1, 2, 3$ with zero mean and variance σ^2. Then, from Equation (A14), it follows that

$$
E\left(\left|{}^2\text{FDO}(Z)\right|\right) = \frac{\sigma}{N^2 d^2}\sqrt{6}\sqrt{\frac{\pi}{2}} = \frac{\sigma}{N^2 d^2}\sqrt{3\pi}. \tag{A18}
$$